



Physical and photo-electrochemical properties of the spinel SrFe₂O₄: application to hydrogen production under visible light

S. Attia¹, N. Helaili^{1,*}, G. Rekhila¹, Y. Bessekhoud^{1,2}, and M. Trari^{1,*}

¹Laboratory of Storage and Valorization of Renewable Energies, Faculty of Chemistry (USTHB), BP 32, 16111 Algiers, Algeria

²National Veterinary School, BP 161-El Harrach, Algiers, Algeria

Received: 11 October 2021

Accepted: 12 February 2022

Published online:

12 March 2022

© The Author(s), under exclusive licence to Springer Science+Business Media, LLC, part of Springer Nature 2022

ABSTRACT

SrFe₂O₄ prepared by sol–gel method after annealing at 800 °C crystallizes in a normal spinel structure. The structural, morphological, magnetic, optical, transport, and photo-electrochemical properties were systematically investigated. The sol–gel permits to have nanocrystallites with an average size of ~ 30 nm. The UV–Visible diffuse reflectance analysis gives a direct transition of 1.80 eV, resulting from the Fe³⁺: 3d orbital splitting in octahedral site. Such degeneracy lifting into (t_{2g}–e_g) levels is properly matched to the sun spectrum. The capacitance–potential (C⁻² – E) characteristic of SrFe₂O₄ plotted in basic electrolyte (KOH 0.1 M) exhibits p-type compartment with a flat band potential of (E_{fb}) of 0.01 V_{SCE}, a holes density (N_A) of 1.4 × 10¹⁵ cm⁻³, and an extended space charge region of 0.9 μm. The electrochemical impedance spectroscopy exhibits a semicircle characteristic of the charge transfer whose diameter decreases under irradiation, thus supporting the semiconducting character of SrFe₂O₄. The electrons in the conduction band (– 1.70 V) have a high reducing ability and cathodically positioned with respect to the H₂O/H₂ level, thus producing H₂ evolution under visible light illumination with a concomitant oxidation of SO₃²⁻/S₂O₆²⁻. The best activity occurs at pH ~ 11 with H₂ evolution rate of 35 μmol mn⁻¹ g⁻¹ and a quantum yield of 1.8% under visible light (29 mW cm⁻²).

1 Introduction

The fossil energy reserves will soon start declining and the photo-electrochemical (PEC) conversion of visible light to electrical and/or chemical energy continues to attract a much attention in the scientific community

[1–3]. Algeria has a high solar potential with an annual insolation of ~ 3200 h and an average solar constant exceeding 1200 W m⁻² (South). However, the intermittence of this energy requires its storage to be released on demand. In this respect, hydrogen with environmentally friendly characteristic is suitable for

Address correspondence to E-mail: nassimahelaili@yahoo.fr; mtrari@usthb.dz

long-term storage with a capacity of $28,540 \text{ cal g}^{-1}$. It can be produced photo-electrochemically and considerable works have been focused on ferromagnetic materials active under UV–Visible light, and the $3d$ metal-based oxides remain privileged because of their chemical stability, high saturation magnetization, thermal properties, and facile synthesis [4–9] compared to sulfide. However, many of them suffer from limitations including a wide gap (E_g), due to the crystalline structure with a valence band (VB) made up of $O^{2-}:2p$ orbital, while the conduction band (CB) derives mostly from metal character [10]. This drawback can be overcome by raising the energy of VB and this occurs by introduction of cationic orbital, which not only decreases the gap but maintains a high reducing ability of CB. In this category, the spinel magnetic nanomaterials MFe_2O_4 ($M=\text{Sr, Te, Ni, Co, etc.}$) continue to attract a growing interest in electronic, optic, magnetic resonance, biosensors, and photocatalysis [11–20] due to their magnetism and absorption over the visible region. In addition, they have pH-independent double layer through which the potential of H_2O/H_2 couple, which varies by $\sim 60 \text{ mV pH}^{-1}$, can be judiciously located. This constitutes a further advantage to have an optimal band bending ($\sim 0.4 \text{ V}$) at the semiconductor/electrolyte junction [21].

On the other hand, the preparation of nanocrystallites is attractive for small polaron oxides with a low carriers' mobility [22], and the spinels were the object of nano-sized effect inquiry [23, 24]. Hence, the conversion of the incident light to electrical current or chemical energy increases with decreasing the crystallite size till it becomes comparable with both the diffusion length of the minority carriers and the light preparation (α^{-1}_λ), where α_λ is the absorption coefficient which depends on the wavelength (λ) [25]. In such a case, the electrons have a high probability to reach the liquid phase to reduce water into hydrogen [26, 27].

The main goal in photocatalysis is to produce large surface areas with crystallites size as small as possible and the sol–gel route seems appropriate in such a case. Our approach is then to prepare $SrFe_2O_4$ with nanomorphology of the kind obtained with the spinel $NiFe_2O_4$ [28]. The choice of $SrFe_2O_4$ for the hydrogen production is motivated by the friendly environmental characteristic, chemical inertness in aqueous medium, and absorption over the visible region. To our knowledge, the photo-electrochemical characterization of $SrFe_2O_4$ is missing, and the photocatalytic properties

have been little investigated. The main purpose of this work was to describe the synthesis of $SrFe_2O_4$, to study its optical, magnetic, morphological, and photo-electrochemical properties in order to be applied for the hydrogen production upon visible light irradiation. Hydrogen is reported because of its chemical stability, low cost, and optimal gap. The loss by recombination is minimized by using a hole scavenger, and SO_3^{2-} is appropriate in our case.

2 Experimental

$SrFe_2O_4$ was synthesized by sol–gel method from $Sr(NO_3)_2$ (Merck, 99%) and $Fe(NO_3)_3 \cdot 9H_2O$ (Flucka, > 98%), dehydrated in a dessicator under static vacuum for several days. The stoichiometric amounts (molar ratio $Sr/Fe:1/2$) were dissolved in distilled water containing agar-agar (1 g L^{-1}); the solution was heated at $70 \text{ }^\circ\text{C}$ (3 h) and $100 \text{ }^\circ\text{C}$ (4 h) until total evaporation. Then, the powder was crushed in an agate mortar and fired at $800 \text{ }^\circ\text{C}$ with intermediate regrinding. The phase has been confirmed by X-ray diffraction (XRD) using a Phillips diffractometer with $Cu \text{ K}\alpha$ radiation ($\lambda = 0.15418 \text{ nm}$) in the 2θ range ($20^\circ\text{--}80^\circ$).

The FTIR spectrum was performed and plotted with a Bruker Alpha (P1000) spectrometer in the range ($400\text{--}4000 \text{ cm}^{-1}$). The X-ray photoelectron spectroscopy (XPS) was performed with Source Gun AA $< \hat{E} = X\text{-Ray } 000 \text{ } 350 \mu\text{m}\text{--FG ON}$ ($350 \mu\text{m}$). The calibration was made by considering the $C1s$ peak (289.4 eV). The SEM images were visualized with a Jeol JSM-7610 F equipped with a Noran EDS detector. The N_2 adsorption–desorption isotherms were obtained by BET surface area analyzer (ASAP 2010 V5.02). The magnetic measurement was carried out at room temperature by using a Vibrating Sample Magnetometer (Microsense easy VSM software) in a magnetic field range $\pm 24,000 \text{ Oe}$ which gives the variation among the applied field H and magnetization M .

The band gap (E_g) of $SrFe_2O_4$ was determined from the diffuse reflectance using a UV–Visible spectrophotometer (Model: Specord 200 Plus) and polytetrafluoroethylene as reference. The pellets, sintered at $850 \text{ }^\circ\text{C}$, were electrically contacted to a copper wire with silver paint; the electrical conductivity was measured by the two probe method using GW Instek equipment (GDM 8255A). The data were accurate

to $\pm 5 \Omega \text{ cm}$, and the temperature was controlled with a Cr–Al thermocouple.

The photo-electrochemical study was done in a standard Pyrex cell; the pellets were encapsulated in glass tubes with insulating araldite, leaving a geometric surface area of 1.12 cm^2 . A PGZ301 Potentiostat was employed for the acquisition of electrochemical data; a saturated calomel electrode (SCE) and Pt foil were used as reference and auxiliary electrodes, respectively. The electrochemical impedance spectroscopy (EIS) was performed over the frequency range (1 mHz–100 kHz), while the Mott–Schottky characteristic was plotted at a frequency of 10 kHz. All experiments were initiated after stabilization of the open circuit potential (OCP).

The photocatalytic tests were carried in a water-cooled Pyrex reactor housing three tungsten lamps ($3 \times 200 \text{ W}$); the flux intensity (29 mW cm^{-2}) was measured with a digital light meter (Testo 545). The temperature was maintained at $50 (\pm 1 \text{ }^\circ\text{C})$ thanks to a thermo-stated bath. SrFe_2O_4 powder (200 mg) was immersed in 200 mL of SO_3^{2-} (0.025 M) solution, and the pH was adjusted by the addition of KOH. The powder was uniformly dispersed under moderate agitation at 210 rpm to occupy the whole reaction space and to preclude the vortex phenomenon. The solution was bubbled by N_2 gas at a purging rate of 10 mL mn^{-1} ; after 35 min, the light was switched on. Hydrogen was qualitatively identified by gas chromatography (Agilent Technology 7890A); because of its low solubility, the amount was quantified volumetrically in a graduated burette by water displacement due to the pressure produced inside the reactor.

3 Results and discussion

The synthesis of oxides by solid state reaction requires high temperatures, leading to irregular and large crystallites with low active surface areas. By contrast, the sol–gel route produces more or less homogenous powder with a narrow size distribution [29]. The XRD pattern of SrFe_2O_4 (Fig. 1) is characteristic of a single phase crystallizing in a spinel structure; the peaks are indexed with a cubic symmetry in agreement with the JCPDS Card N° 001-1027. The lattice constant (a) and spacing between crystal planes (d_{hkl}) are linked by the relation [16, 30]:

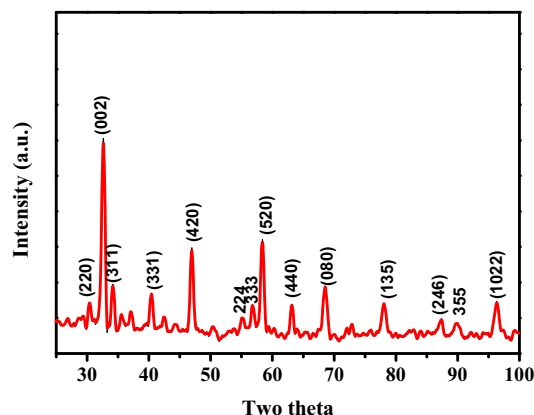


Fig. 1 X-ray diffraction pattern of SrFe_2O_4 prepared by sol–gel route and calcined at $800 \text{ }^\circ\text{C}$

$$a = d_{hkl} \sqrt{h^2 + k^2 + l^2} \quad (1)$$

We do not detect any peak due to secondary phase like the deficient perovskite $\text{Sr}_2\text{Fe}_2\text{O}_5$ [31] or SrO which converts into $\text{Sr}(\text{OH})_2$ when exposed to free atmosphere. The sharp peaks indicate small crystallites size ($D = 31 \text{ nm}$) (β in rd., = $K\lambda/\beta\cos\theta$), where K ($= 0.94$) is the shape factor and β (rd.) is the broadening at half maximum. The dislocation density (δ) was calculated with the help of the value of crystallite size using the following relations: [32]

$$\delta = \frac{1}{D^2} \quad (2)$$

$$V = a^3 (\text{\AA}^3) \quad (3)$$

An active surface area of SrFe_2O_4 was calculated from the relation ($= 6/\rho_{\text{XRD}}D$), where ρ_{XRD} is the theoretical density (5.36 g cm^3). The lattice constant, unit cell volume, crystallite size, and dislocation density of the spinel oxide are given in Table 1.

The FTIR spectroscopy is a useful technique for identifying the chemical absorption. The two broad bands in the spectrum are assigned to metal–oxygen of the ferrite spinel (Fig. 2). The highest one, ν_1 in the range ($800\text{--}600 \text{ cm}^{-1}$), corresponds to stretching vibrations of the metal in tetrahedral site (T_d), M_t tetra

Table 1 Lattice constant (a), unit cell volume (V), crystallite size (D), and the dislocation density of SrFe_2O_4 nanoparticle

Parameters	a (\AA)	V (\AA^3)	D (nm)	$\delta \nu 10^{-3}$ (lines/ nm^2)
SrFe_2O_4	5.50	166.375	30.89	1.048

MO, while the lowest ν_2 band in the region (550–400 cm^{-1}) is attributed to octahedral–metal stretching (O_h), Mocta MO [33–36]. The SEM micrographs of SrFe_2O_4 (Fig. 3) show give grains morphology. Some grains are necked in shape, due to the diffusion among the particles during sintering. This means that the smaller particles join together to form the larger particles [37]. Images show an intense and irregular dispersion of conglomerates without specific morphology [38]. Agglomeration occurs between the particles, due to the dipole–dipole interaction among the particles [39], and the elemental composition (Fig. 3) gives 38.56% of Sr, 32.18% of O, and 24.95% of Fe.

The XPS analysis was used to determine the composition and surface valence states (Fig. 4). The characteristic lines of O, Sr, and Fe of the spinel are observed, and the carbon peak C 1s (289.23 eV) is due to the grid used for analysis and/or CO_2 adsorption. The analysis of the curves fitting revealed that Sr^{2+} and Fe^{3+} species are located in different sites (tetrahedral-A and octahedral-B). The deconvoluted spectrum of O 1s orbital (Fig. 4a) shows one typical peak due to chemical state of oxygen (531.5 eV) in Sr–O–Fe. Figure 4b displays the spectrum of Sr 3d orbital with two peaks at 135.28 and 133.4 eV assigned to Sr 3d_{3/2} and Sr 3d_{5/2} orbitals, respectively. Figure 4c illustrates the spectrum of Fe 2p orbital, where the peaks 724.28, 710.78, and 718.68 eV correspond to Fe 2p_{1/2} and Fe 2p_{3/2} orbitals respectively [47]. The peaks at 710 eV and 718.68 eV are assigned to the presence of Fe^{3+} located respectively in the A- and B-sites, indicating that Fe^{3+}

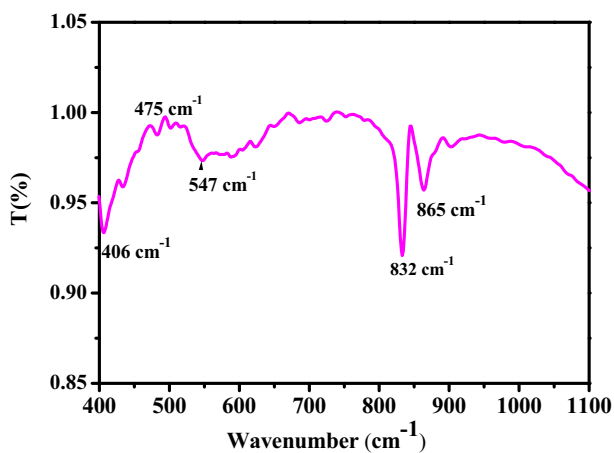


Fig. 2 FTIR spectrum of SrFe_2O_4 prepared by sol–gel route

favors rather octahedral coordination in the spinel structure.

The N_2 adsorption–desorption isotherm of SrFe_2O_4 (Fig. 5) gives a specific surface area of 26 $\text{m}^2 \text{g}^{-1}$.

The magnetic properties of SrFe_2O_4 , such as saturation magnetization (M_s), residual magnetization (M_r), and coercive field (H_c), as well as the squareness ratio M_r/M_s , were measured at room temperature in a magnetic field ranging from $-24,000$ to $24,000$ Oe (Fig. 6 and Table 2). An hysteresis loop was observed from the magnetization curve $M(H)$, characteristic of a hard ferrite with ferromagnetic behavior and a Curie temperature above 300 K, due to the magnetization M_r (6.045 emu/g) when the field (H) is zero. The significant field H_c (3892 Oe) makes this spinel ferrite resistant to demagnetization [40, 41]. Our sample with a squareness ratio of 0.47 (< 0.5) has a single domain structure, whereas materials with a ratio greater than 0.5 have a multi-domain structure [42]. So, we conclude that the prepared ferrite exhibits better magnetic properties, a desired property in photocatalysis.

The optical gap (E_g), vital in the photo-electrochemical conversion, quantifies the solar flux converted into useful energies. It is determined from the diffuse reflectance (R) by using the relation:

$$(\alpha_\lambda h\nu)^m = (E_g - h\nu) \quad (4)$$

The exponent m is equal to 0.5 or 2, respectively, for indirect and direct transitions. The E_g value (1.85 eV) is obtained by extrapolating the line $(\alpha_\lambda h\nu)^2$ to the energy-axis (Fig. 7), and the transition is directly allowed indicating that the top of the valence band (VB) coincides and the bottom of the conduction band (CB) is with no phonon assistance. The E_g value is close to that obtained elsewhere [43]; α_λ (cm^{-1}) is the absorption coefficient and its inverse represents the light penetration of the monochromatic light (λ). The gap (E_g) results from the octahedral crystal field splitting of Fe^{3+} : $3d$ orbital into three lower energy levels t_{2g} and two upper levels e_g . It describes the lifting of orbital degeneracy in the Fe^{3+} complexes due to the presence of oxygen octahedra and the strength of the Fe–O bond.

The semi-conductivity is a required property in photocatalysis and depends on the extent of deviation from the stoichiometry. The Hall effect cannot be measured, indicating a resistive oxide ($\sigma_{300\text{K}} < 10^{-6} \Omega^{-1} \text{cm}^{-1}$) with a low holes density (see below.) The

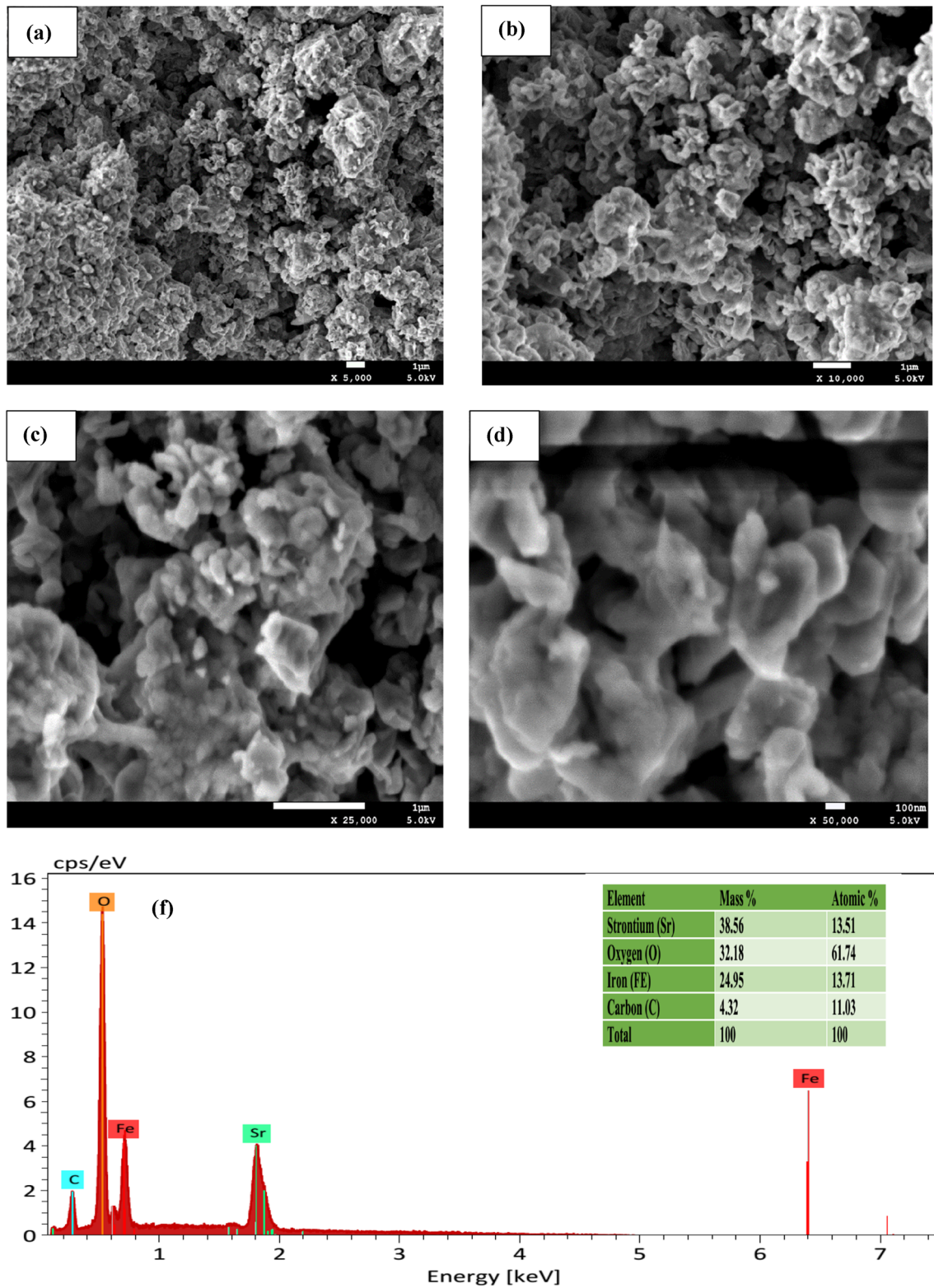


Fig. 3 SEM images showing the morphology of SrFe_2O_4 at different magnifications. **a** $\times 5000$, **b** $\times 10,000$, **c** $\times 25,000$, **d** $\times 50,000$, and **f** EDX composition of SrFe_2O_4

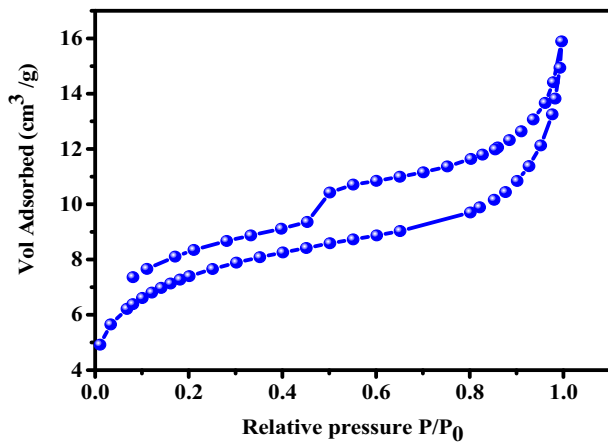


Fig. 5 N₂ adsorption–desorption isotherms of the spinel SrFe₂O₄ at –196 K

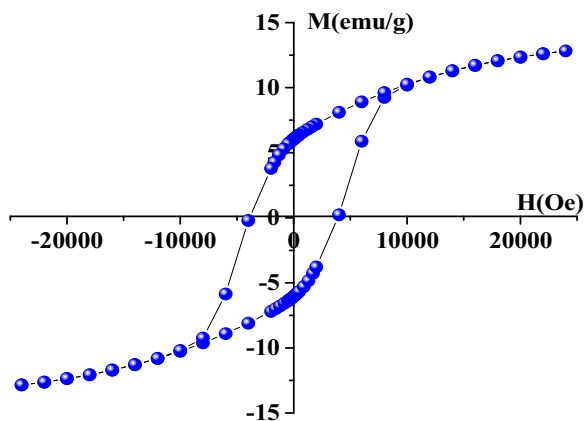


Fig. 6 Magnetic hysteresis loop for SrFe₂O₄ prepared by sol–gel method

Table 2 Magnetic parameters for SrFe₂O₄ spinel ferrite

Sample	Saturation magnetization M_s (emu/g)	Remanent magnetization M_r (emu/g)	Coercivity H_c	M_r/M_s
SrFe ₂ O ₄	12.84	6.045	3892.62	0.47

capacitance–potential ($C^{-2} - E$) plot is used for a reliable determination of CB:

$$C^{-2} = \{2/\epsilon\epsilon_0 N_A\} \{E - E_{fb}\} \quad (5)$$

All symbols have their usual significations. The flat band potential ($E_{fb} = 0.01$ V) is simply deduced by extrapolating the linear plot to infinite capacitance ($C^{-2} = 0$) (Fig. 10), and is equivalent to the built-in potential in the solid state. The negative slope confirms the *p*-type conductivity where the majority carriers are holes. The semi-logarithmic (Fig. 11) confirms the electrochemical stability of the

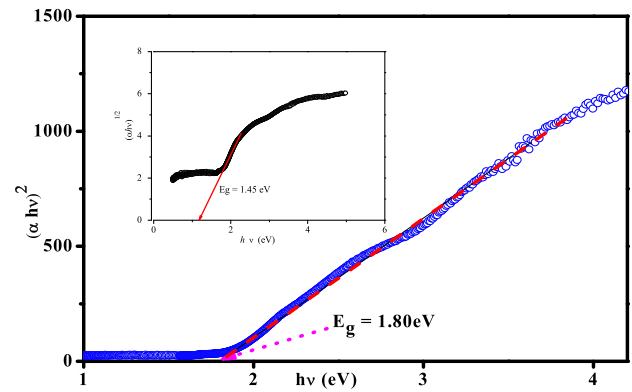


Fig. 7 Direct and indirect optical transitions of SrFe₂O₄ prepared by sol–gel route

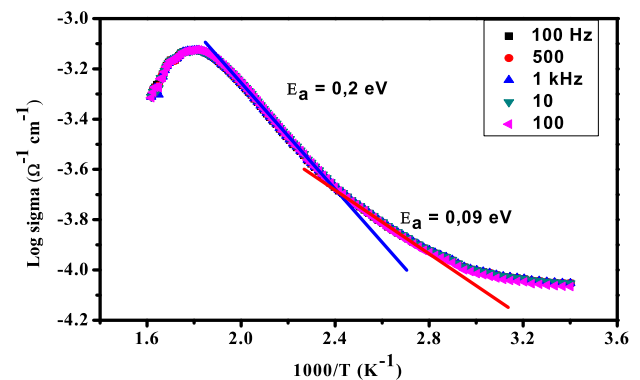


Fig. 8 Logarithm of the electrical conductivity of SrFe₂O₄ vs. reciprocal temperature

spinel. The energy of CB ($= e \times E_{fb} + E_a - E_g$) is positioned at 3.05 ± 0.10 V below vacuum [44] (Fig. 12). It corresponds to a potential of -1.70 V, more cathodic than that of hydrogen and should trigger the H₂ evolution under visible illumination. The valence band (VB: 4.85 eV/ 0.1 V) is simply deduced from the relation:

$$E_{VB} = E_{CB} - E_g \quad (6)$$

EIS analysis quantifies the different contributions of the solid/liquid junction and provides information on the electron transfer mechanism. It is a non-stationary

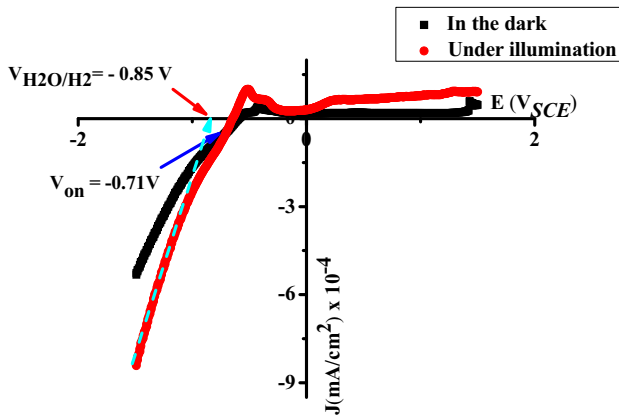


Fig. 9 The $J(E)$ plots of SrFe_2O_4 electrode in KOH solution (0.5 M) under N_2 -atmosphere in the dark and under visible irradiation. Scan rate 10 mV/s

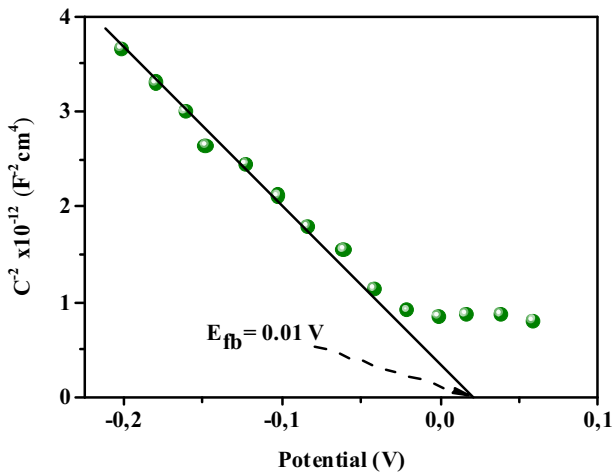


Fig. 10 The Mott–Schottky characteristic of SrFe_2O_4 plotted in KOH solution at a frequency of 10 kHz

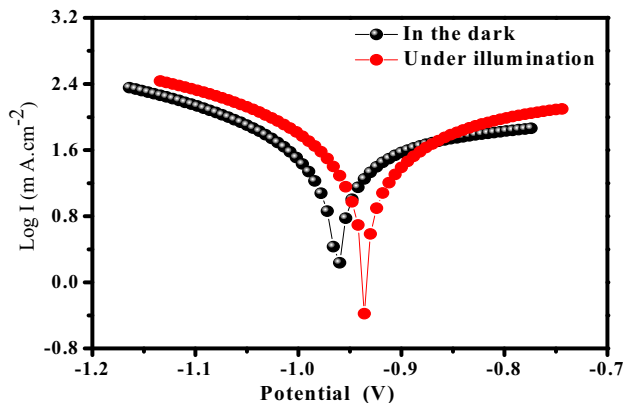


Fig. 11 Semi logarithmic plots of SrFe_2O_4 in KOH (10^{-2} M) solution under N_2 bubbling; scan rate 10 mV/s

technique and the excitation with small amplitude does not modify the system, thus permitting repeated tests at the free potential (Fig. 12). The occurrence of two loops in the EIS plot of SrFe_2O_4 is due to the bulk and grains boundaries. As expected, the diameter of the first semicircle decreases under illumination (Fig. 13), thus corroborating the semiconducting behavior. The EIS diagram does not show a straight line at low frequencies, indicating the absence of Warburg impedance. Such observation agrees with the existence of a plateau region in the $J(E)$ characteristics. The center of the semicircle is located below the real axis, due to a deviation from a pure capacitive behavior with the existence of a constant phase element (CPE). An electrical equivalent circuit is suggested by fitting the data with the Z-View software.

4 Photocatalysis

The oxide is not deliberately doped and the low holes density extends the space charge region up to $\sim 0.9 \mu\text{m}$, allowing the participation of the most electron/hole (e^-/h^+) pairs in the photoactivity. The distance traveled by the electrons to reach the interface decreases, and these electrons are then captured by the water adsorbed on the surface inside the pores.

As mentioned above, SrFe_2O_4 is a small polaron semiconductor with a low carrier mobility ($\mu_h \sim 10^{-6} \text{ cm}^2 \text{ V}^{-1} \text{ s}^{-1}$), the latter is calculated from the relation ($\sigma = \mu e N_A$). Therefore, the adopted strategy was to reduce the crystallite size below diffusion length, and the advantage of sol–gel is to produce small crystallites with increased specific surface. Nanoparticles with sizes (D) in the range (30–50 nm) give enhanced active

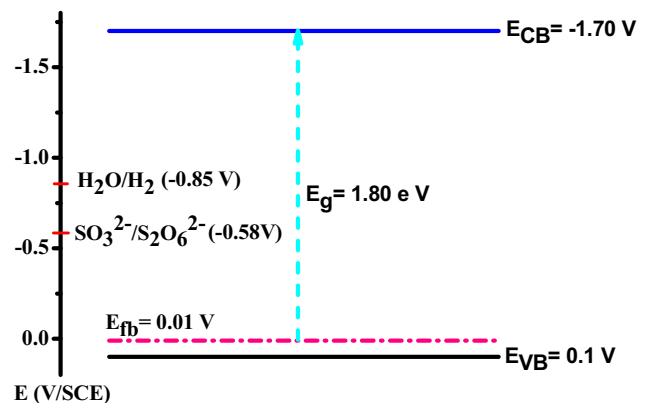


Fig. 12 Energetic diagram of the junction $\text{SrFe}_2\text{O}_4/\text{KOH}$ electrolyte, given in the electrochemical scale at pH 7

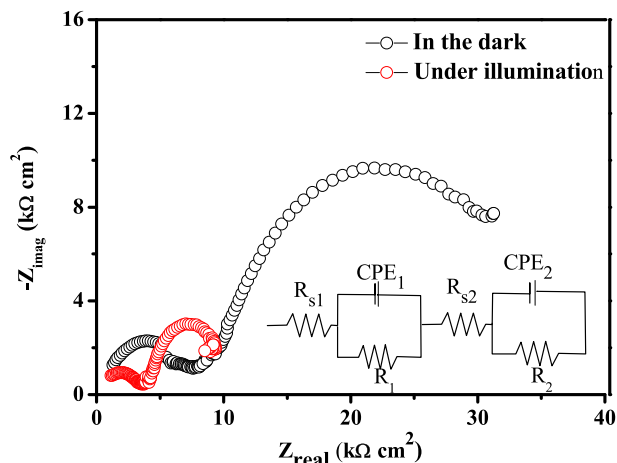


Fig. 13 The complex impedance spectroscopy of SrFe₂O₄ in KOH solution plotted in the dark and under illumination. Inset: the equivalent electrical circuit

surface area with more photocatalytic sites. A specific surface area of $\sim 26 \text{ m}^2 \text{ g}^{-1}$ was evaluated from the BET analysis. The electrochemical characterization revealed chemical stability in KOH electrolyte under irradiation. The excited electrons have a cathodic potential, sufficient to convert water into hydrogen.

Hydrogen is a nonpolluting fuel with no greenhouse gases emission and could bring a partial solution for the clean energy supply and environmental protection [45, 46]. The maximum photovoltage produced by a semiconductor under irradiation cannot exceed E_g/e . Accordingly, to split water into oxygen and hydrogen, a gap greater than 2.2 eV is required because of the high O₂-over-voltage [48]. So, O₂ cannot be evolved through by a valence band process and a reducing agent must be used to capture the photoholes; this improves the charges separation and protects the oxide against the photo-oxidation [49]. Figure 12 depicts a possible photocatalytic reaction mechanism of SrFe₂O₄. The electrons are excited to the conduction band, leaving holes on the valence band (8). The photogenerated electrons focalized to H₂O molecules to be reduced into H₂, while the holes react on the surface with SO₃²⁻. On the other side, the pH has a great influence in photo-electrochemistry. The results (Fig. 14) show that SrFe₂O₄ is active at various pHs, leading to different performances. The best activity is obtained at pH ~ 11 , followed by pH 7 and 3 because the potential $E(\text{H}_2)$ moves toward the cathodic direction, producing an optimal interfacial band bending at pH ~ 11 with a complete separation of (e⁻/h⁺) pairs. The H₂

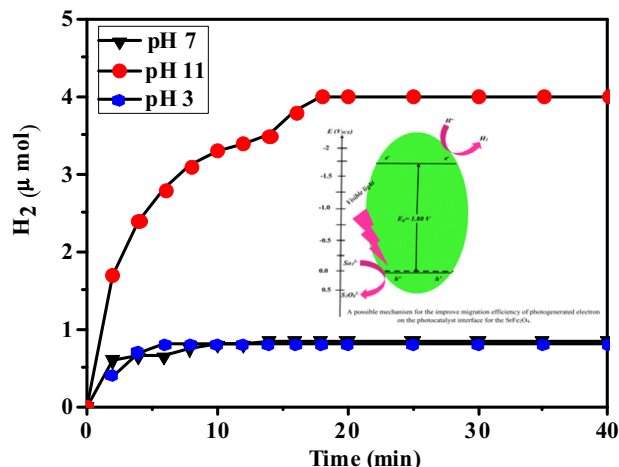
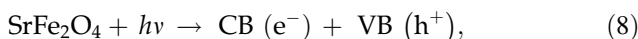


Fig. 14 Volume of evolved H₂ on SrFe₂O₄ in alkaline medium (KOH, 10⁻² M + Na₂SO₃, 0.025 M)

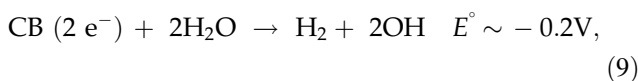
formation needs two electrons, and the conversion efficiency is given by the relation:

$$\eta = 2 \times \left\{ \text{number of H}_2 \text{ mol s}^{-1} \right\} / \left\{ \text{photons flux s}^{-1} \right\} \quad (7)$$

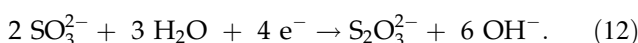
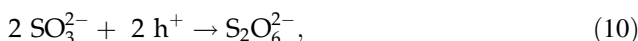
Water is reduced into hydrogen, while SO₃²⁻ is concomitantly oxidized according to the following sequences:



Cathodic pole



Anodic pole



The photocatalytic hydrogen formation occurs in ~ 20 min above which a net tendency to saturation was observed. This indicates that the reaction (11) is disfavored, otherwise the saturation should not be observed since the sulfate with a redox potential of ~ 2 V is stable and does not compete with photo-electrons. Therefore, one can conclude that the deactivation of the catalyst by H₂-adsorption is due to competitive reaction (12) where the thiosulfate S₂O₃²⁻ consumes the photo-electrons. The saturation of catalytic sites also accounts for the regression of the

photoactivity. More interestingly, the initial activity of the catalyst powder is completely restored during the second cycle.

Our research suggests that pursuing the synthesis of spinel AFe_2O_4 by Sol–Gel method, A denotes a alkaline earth metals. This is the goal to study the impact on the physico-chemical properties on the H_2 photo-production.

5 Conclusion

The spinel SrFe_2O_4 was synthesized by sol–gel route with an average crystallite size of 40 nm. It is an attractive photocatalyst, due to its chemical stability, low cost, and optical gap of ~ 1.8 eV close to the optimal conversion value. The electronic bands are made up of $3d$: orbital with a high reducing ability and appropriately positioned with respect to H_2 level. The formation of cubic phase was confirmed by XRD analysis. The irregular and intense morphology of the spinel was observed by the SEM images. The VSM reveals a hard ferrite with a ferromagnetic behavior due to the presence of the magnetization M_r (6.045 emu g^{-1}) for a zero applied magnetic field. The XPS analysis revealed that Sr^{2+} and Fe^{3+} are located respectively in four- and six-fold coordination. The $d-d$ optical transition comes from the crystal field splitting of Fe^{3+} : $3d$ in octahedral site. The thermal dependence of the electrical conductivity showed a semiconductor behavior with an activation energy of 0.09 eV. The capacitance measurement gave a flat band potential of 0.01 V_{SCE} and a hole density of $1.4 \times 10^{15} \text{ cm}^{-3}$. The electrochemical characterization revealed chemical stability and the potentiality of SrFe_2O_4 in photocatalysis. Indeed, the spinel was tested for the hydrogen formation under illumination and the best activity occurs at $\text{pH} \sim 11$ with H_2 evolution rate of $35 \mu\text{mol mn}^{-1} \text{ g}^{-1}$ and a quantum yield of 1.8%. Therefore, the oxidation of sulfite permits to protect the spinel against photo-corrosion and to improve the charges separation. The saturation over time course evolution is due to the competition reduction of thio-sulfate $\text{S}_2\text{O}_3^{2-}$ and occupation of photo-electrochemical sites by adsorbed hydrogen.

Acknowledgements

The authors are indebted to Dr R. Brahimi (USTHB University) for her technical assistance. The authors

also thank the financial support by the Faculty of Chemistry (Algiers).

Author contributions

NH supervised the work, NH and MT discussed the results and wrote the manuscript. SA and NH performed the experiments, GR did the application part. NH and MT and YB discussed the results.

Data availability

All data generated or analyzed during this study are included in this published article.

Declarations

Conflict of interest All authors declare that they have no financial or non-financial interest in this manuscript.

References

- Zheng HQ, Wang XB, Hu JY, Zhao JA, Du CX, Fan YT et al (2016) Photo-catalytic H_2 evolution, structural effect and electron transfer mechanism based on four novel $[\text{2Fe2S}]$ model complexes by photochemical splitting water. Sol. Energy 132:373–385. <https://doi.org/10.1016/j.solener.2016.03.010>
- Jin-hui Z (2012) Research on UV/ TiO_2 photocatalytic oxidation of organic matter in drinking water and its influencing factors. Procedia Environ. Sci. 12:445–452. <https://doi.org/10.1016/j.proenv.2012.01.302>
- Rekhila G, Gabes Y, Bessekhoud Y, Trari M (2018) Hydrogen production under visible illumination on the spinel NiMn_2O_4 prepared by sol gel. Sol. Energy 166:220–225. <https://doi.org/10.1016/j.solener.2018.02.064>
- Kaizra S, Louafi Y, Bellal B, Trari M, Rekhila G (2015) Electrochemical growth of tin(II) oxide films: application in photocatalytic degradation of methylene blue. Mater. Sci. Semicond. Process. 30:554–560. <https://doi.org/10.1016/j.mssp.2014.10.045>
- Roumila Y, Abdmeziem K, Rekhila G, Trari M (2016) Semiconducting properties of hydrothermally synthesized libethenite application to orange G photodegradation. Mater Sci Semicond Process. <https://doi.org/10.1016/j.mssp.2015.10.018>

6. Rekhila G, Bessekhoud Y, Trari M (2016) Synthesis and characterization of the spinel ZnFe₂O₄, application to the chromate reduction under visible light. *Environ Technol Innov.* <https://doi.org/10.1016/j.eti.2016.01.007>
7. Vijayalakshmi S, Elaiyappillai E, Johnson PM et al (2020) Multifunctional magnetic CoFe₂O₄ nanoparticles for the photocatalytic discoloration of aqueous methyl violet dye and energy storage applications. *J. Mater. Sci.: Mater. Electron.* 31:10738–10749. <https://doi.org/10.1007/s10854-020-03624-z>
8. Kharat PB, More SD, Somvanshi SB et al (2019) Exploration of thermoacoustics behavior of water based nickel ferrite nanofluids by ultrasonic velocity method. *J. Mater. Sci.: Mater. Electron.* 30:6564–6574. <https://doi.org/10.1007/s10854-019-00963-4>
9. Kulkarni GD, Khedkar MV, Somvanshi SB, Borade RM, More SD, Jadhav KM (2021) Green synthesis and investigations of structural, cation distribution, morphological, and magnetic properties of nanoscale nickel ferrites: the effect of green fuel proportion. *Phase Trans.* 94(12):994–1005. <https://doi.org/10.1080/01411594.2021.1993221>
10. Dib K, Brahimi R, Bessekhoud Y, Tayebi N, Trari M (2016) Structural, optical and transport properties of S_xZnO. *Mater. Sci. Semicond. Process.* 48:52–59. <https://doi.org/10.1016/j.mssp.2016.03.010>
11. Xu Q, Li R, Wang C, Yuan D (2017) Visible-light photocatalytic reduction of Cr(VI) using nano-sized delafossite (CuFeO₂) synthesized by hydrothermal method. *J. Alloy. Compd.* 723:441–447. <https://doi.org/10.1016/j.jallcom.2017.06.243>
12. Jadhav SA, Khedkar MV, Somvanshi SB, Jadhav KM (2021) Magnetically retrievable nanoscale nickel ferrites: an active photocatalyst for toxic dye removal applications. *Ceram Int* 47(20):28059–29534. <https://doi.org/10.1016/j.ceramint.2021.07.021>
13. Kharat PB, Somvanshi SB, Khirade PP, Jadhav KM (2020) Induction heating analysis of surface-functionalized nanoscale CoFe₂O₄ for magnetic fluid hyperthermia toward noninvasive cancer treatment. *ACS Omega* 5(36):23378–23384. <https://doi.org/10.1021/acsomega.0c03332>
14. Somvanshi SB, Kharat PB, Saraf TS, Somvanshi SB, Shejul SB, Jadhav KM (2020) Multifunctional nano magnetic particles assisted viral RNA-extraction protocol for potential detection of COVID-19. *Mater Res Innov.* <https://doi.org/10.1080/14328917.2020.1769350>
15. Patade SR, Andhare DD, Somvanshi SB, Kharat PB, Jadhav KM (2020) Effect of zinc doping on water-based manganese ferrite nanofluids for magnetic hyperthermia application. *AIP Conf. Proc.* 2265:030557. <https://doi.org/10.1063/5.0017051>
16. Bhosale AB, Somvanshi SB, Murumkar VD, Jadhav KM (2020) Influential incorporation of RE metal ion (Dy³⁺) in yttrium iron garnet (YIG) nanoparticles: magnetic, electrical and dielectric behavior. *Ceram. Int.* 46:15372–15378. <https://doi.org/10.1016/j.ceramint.2020.03.081>
17. Patade SR, Andhare DD, Somvanshi SB, Jadhav SA, Khedkar MV, Jadhav KM (2020) Self-heating evaluation of superparamagnetic MnFe₂O₄ nanoparticles for magnetic fluid hyperthermia application towards cancer treatment. *Ceram. Int.* 46:1625576–1625583. <https://doi.org/10.1016/j.ceramint.2020.07.029>
18. Kharat PB, Somvanshi SB, Kounsalye JS, Deshmukh SS, Khirade PP, Jadhav KM (2018) Temperature dependent viscosity of cobalt ferrite/ethylene glycol ferrofluids. *AIP Conf. Proc.* 1942:050044. <https://doi.org/10.1063/1.5028675>
19. Kharat PB et al (2020) *J. Phys.: Conf. Ser.* 1644:012028. <https://doi.org/10.1088/1742-6596/1644/1/012028>
20. Hake RR (1967) upper-critical-field limits for bulk type-II superconductors. *Appl. Phys. Lett.* 10:189. <https://doi.org/10.1063/1.1754905>
21. Gerischer H (1990) The impact of semiconductors on the concepts of electrochemistry. *Electrochim. Acta* 35(11–12): 1677–1699. [https://doi.org/10.1016/0013-4686\(90\)87067-C](https://doi.org/10.1016/0013-4686(90)87067-C)
22. Meziani D, Rezig A, Rekhila G, Bellal B, Trari M (2014) Hydrogen evolution under visible light over LaCoO₃ prepared by chemical route. *Energy Convers. Manag.* 82:244–249. <https://doi.org/10.1016/J.ENCONMAN.2014.03.028>
23. Rekhila G, Bessekhoud Y, Trari M (2015) Hydrogen evolution under visible light over the solid solution NiFe_{2-x}Mn_xO₄ prepared by sol gel. *Int. J. Hydrogen Energy* 40:12611–12618. <https://doi.org/10.1016/j.ijhydene.2015.07.109>
24. Ali AM, Emanuelsson EAC, Patterson DA (2011) Conventional versus lattice photocatalysed reactions: implications of the lattice oxygen participation in the liquid phase photocatalytic oxidation with nanostructured ZnO thin films on reaction products and mechanism at both 254nm and 340nm. *Appl. Catal. B* 106:323–336. <https://doi.org/10.1016/j.apcatb.2011.05.033>
25. Brahimi R, Bessekhoud Y, Bouguelia A, Trari M (2007) CuAlO₂/TiO₂ heterojunction applied to visible light H₂ production. *J. Photochem. Photobiol. A* 186:242–247. <https://doi.org/10.1016/j.jphotochem.2006.08.013>
26. Fan T, Chen C, Tang Z, Ni Y, Lu C (2015) Materials Science in Semiconductor Processing Synthesis and characterization of g-C₃N₄/BiFeO₃ composites with an enhanced visible light photocatalytic activity. *Mater. Sci. Semicond. Process.* 40:530–535
27. W. Zhao, D.Y.C. Leung, SC (2019)
28. Rekhila G, Bessekhoud Y, Trari M (2013) Visible light hydrogen production on the novel ferrite NiFe₂O₄ *Int.*

- J. Hydrogen Energy 38:6335–6343. <https://doi.org/10.1016/j.ijhydene.2013.03.087>
29. Rekhila G, Gabes Y, Brahimi R, Bessekhoud Y, Mahroua O, Trari M (2018) Preparation and characterization of the system NiMn₂O₄/TiO₂ by sol–gel: application to the photodegradation of benzamide under visible light. *J. Sol-Gel Sci. Technol.* 85:677–683. <https://doi.org/10.1007/s10971-018-4598-x>
 30. Bharati VA, Somvanshi SB, Humbe AV, Murumkar VD, Sondur VV, Jadhav KM (2020) Influence of trivalent AlCr co-substitution on the structural, morphological and Mossbauer properties of nickel ferrite nanoparticles. *J. Alloy. Compd.* 821:153501. <https://doi.org/10.1016/j.jallcom.2019.153501>
 31. Saib F, Mekiri M, Bellal B, Chibane M, Trari M (2017) Photoelectrochemical properties of the Brownmillerite Sr₂Fe₂O₅: application to electrochemical oxygen evolution. *Russ. J. Phys. Chem.* 91:1562–1570. <https://doi.org/10.1134/S0036024417080295>
 32. Somvanshi SB, Khedkar MV, Kharat PB, Jadhav KM (2020) Influential diamagnetic magnesium (Mg²⁺) ion substitution in nano-spinel zinc ferrite (ZnFe₂O₄): thermal, structural, spectral, optical and physisorption analysis. *Ceram. Int.* 46:8640–8650. <https://doi.org/10.1016/j.ceramint.2019.12.097>
 33. Rekhila G, Trari M (2021) Physical properties of the ferrites NiFe₂– xMnxO₄ (0 ≤ x ≤ 2) prepared by sol–gel method. *J. Mater. Sci.: Mater. Electron.* 32:1897–1906. <https://doi.org/10.1007/s10854-020-04958-4>
 34. Tatarchuk T, Shyichuk A, Sojka Z, Gryboś J, Naushad M, Kotsyubynsky V, Kowalska M, Kwiatkowska-Marks S, Danyliuk N (2021) Green synthesis, structure, cations distribution and bonding characteristics of superparamagnetic cobalt-zinc ferrites nanoparticles for Pb(II) adsorption and magnetic hyperthermia applications. *J. Mol. Liq.* 328. <https://doi.org/10.1016/j.molliq.2021.11537>
 35. Tatarchuk T, Shyichuk A, Trawczyńska I, Yaremiy I, Pędziwiatr AT, Kurzydło P, Gargula R (2020) Spinel cobalt(II) ferrite-chromites as catalysts for H₂O₂ decomposition: synthesis, morphology, cation distribution and antistructure model of active centers formation. *Ceram. Int.* 46:27517–27530. <https://doi.org/10.1016/j.ceramint.2020.07.243>
 36. Tatarchuk T, Naushad M, Tomaszewska J et al (2020) Adsorption of Sr(II) ions and salicylic acid onto magnetic magnesium-zinc ferrites: isotherms and kinetic studies. *Environ. Sci. Pollut. Res.* 27:26681–26693. <https://doi.org/10.1007/s11356-020-09043-1>
 37. Burange NM, Chogule SS, Patil DR, Devan RS, Koleka YD, Chougale BK (2009) *J. Alloy. Compd.* 2009(479):569–573. <https://doi.org/10.1016/j.jallcom.2009.01.004>
 38. Liu X, Zhang T, Zhang L (2018) Microwave-induced catalytic application of magnetically separable strontium ferrite in the degradation of organic dyes: insight into the catalytic mechanism. *Sep. Purif. Technol.* 195:192–198. <https://doi.org/10.1016/j.seppur.2017.12.015>
 39. Li L, Xiang C, Liang X, Hao B (2010) *Synth. Met.* 160:28–34. <https://doi.org/10.1016/j.synthmet.2009.09.026>
 40. Ghalandari A, Taghizadeh M, Rahmani M (2019) Statistical optimization of the biodiesel production process using a magnetic core-mesoporous shell KOH/Fe₃O₄@γ-Al₂O₃ nanocatalyst. *Chem. Eng. Technol.* 42(1):89–99. <https://doi.org/10.1002/ceat.201700658>
 41. Shaikh SF, Mohd Ubaidullah M, Mane RS, Al-Enizi A (2020) Types, synthesis methods and applications of ferrites. In: Mane RS, Jadhav V (eds) *Spinel Ferrite Nanostructures for Energy Storage Devices*. Elsevier, Amsterdam, pp 51–82. <https://doi.org/10.1016/B978-0-12-819237-5.00004-3>
 42. Muthuselvam IP, Bhowmik RN (2010) *J. Magn. Magn. Mater.* 322:767–776. <https://doi.org/10.1016/j.jmmm.2009.10.057>
 43. Azoudj Y, Merzougui Z, Rekhila G, Trari M (2018) The adsorption of HCrO₄– on activated carbon of date pits and its photoreduction on the hetero-system Zn Co₂O₄/TiO₂ *Appl Water Sci* 8:114. <https://doi.org/10.1007/s13201-018-0755-1>
 44. Cherifi K, Rekhila G, Omeiri S, Bessekhoud Y, Trari M (2019) Physical and photoelectrochemical properties of the spinel Zn Cr₂O₄ prepared by sol gel: application to orange II degradation under solar light. *J. Photochem. Photobiol. A* 368:290–295
 45. Abbasi T, Abbasi SA (2010) Biomass energy and the environmental impacts associated with its production and utilization. *Renew. Sustain. Energy Rev.* 14:919–937. <https://doi.org/10.1016/j.rser.2009.11.006>
 46. Tributsch H (2008) Photovoltaic hydrogen generation. *Int. J. Hydrogen Energy* 33:5911–5930. <https://doi.org/10.1016/j.ijhydene.2008.08.017>
 47. Ahmad I, Shah S, Zafar MN, Ashiq MN, Tang W, Jabee U (2020) Synthesis, characterization and charge transport properties of Pr–Ni Co-doped SrFe₂O₄ spinel for high frequency devices applications. *Ceram. Int.* 47:3760–3771. <https://doi.org/10.1016/j.ceramint.2020.09.233>
 48. Abid H, Rekhila G, Ihaddadene FA, Bessekhoud Y, Trari M (2019) Hydrogen evolution under visible light illumination on the solid solution Cd_xZn_{1-x}S prepared by ultrasound-assisted route. *Int. J. Hydrogen Energy* 44:4–11
 49. Shirsath SE, Toksha BG, Jadhav KM (2009) Structural and magnetic properties of In³⁺ substituted NiFe₂O₄ *Mater. Chem. Phys.* 117:163–168. <https://doi.org/10.1016/j.matchemphys.2009.05.027>

Publisher's Note Springer Nature remains neutral with regard to jurisdictional claims in published maps and institutional affiliations.